

Glacial cycles drive variations in the production of oceanic crust

John W. Crowley,^{1,2*} Richard F. Katz,^{1†} Peter Huybers,² Charles H. Langmuir,² Sung-Hyun Park^{3†}

¹Department of Earth Sciences, University of Oxford, Oxford, UK. ²Department of Earth and Planetary Sciences, Harvard University, Cambridge, USA. ³Division of Polar Earth-System Sciences, Korea Polar Research Institute, Incheon, Korea.

*Present address: Engineering Seismology Group Canada, Kingston, Canada.

†Corresponding author. E-mail: Richard.Katz@earth.ox.ac.uk (R.F.K.); shpark314@kopri.re.kr (S.-H. P.)

Glacial cycles redistribute water between oceans and continents causing pressure changes in the upper mantle, with consequences for melting of Earth's interior. Using Plio-Pleistocene sea-level variations as a forcing function, theoretical models of mid-ocean ridge dynamics that include melt transport predict temporal variations in crustal thickness of hundreds of meters. New bathymetry from the Australian-Antarctic ridge shows statistically significant spectral energy near the Milankovitch periods of 23, 41, and 100 ky, consistent with model predictions. These results suggest that abyssal hills, one of the most common bathymetric features on Earth, record the magmatic response to changes in sea level. The models and data support a link between glacial cycles at the surface and mantle melting at depth, recorded in the bathymetric fabric of the sea floor.

The bathymetry of the sea floor has strikingly regular variations around intermediate and fast-spreading ocean ridges. Parallel to the ridge are long, linear features with quasi-regular spacing called abyssal hills (1). High resolution mapping of the sea floor over the past few decades [e.g., (2–4)] has shown that these hills are among the most common topographic features of the planet, populating the sea floor over ~50,000 km of ridge length. Hypothesized models for these features include extensional faulting parallel to the ridge (3), variations in the magmatic budget of ridge volcanoes (5), and variation in mantle melting under ridges due to sea-level change associated with glacial cycles (6). This latter model stems from the fact that glacial-interglacial variations transfer about 5×10^{19} kg of water between the oceans and the continents. This mass redistribution translates to sea-level variations of ~100 m and modifies the lithostatic pressure beneath the entire ocean. Because mantle melting beneath ridges is driven by depressurization, ocean ridge volcanism should respond to sea-level changes, potentially leading to changes in the thickness and elevation of oceanic crust.

Plate spreading at mid-ocean ridges draws mantle flow upward beneath the ridge; rising parcels of mantle experience decreasing pressure and hence decreasing melting point, causing partial melting. Mantle upwelling rates are about 3 cm/year on average, while sea level change during the last deglaciation was at a mean rate of 1 cm/year over 10,000 years. Because water has one third the density of

rock, sea-level changes would modify the depressurization rate associated with upwelling by $\pm 10\%$, with corresponding effects on the rate of melt production. Mantle upwelling rate scales with the mid-ocean ridge spreading rate, but the rate of sea level change over the global mid-ocean ridge system is roughly uniform. On this basis, previous workers inferred that the relative effect of sea level change should scale inversely with spreading rate, reaching a maximum at the slowest rates (6). An elaboration of this model with parameterized melt transport gave a similar scaling (7).

To test these qualitative inferences, we investigated the crustal response to sea-level change using a model that computes mantle flow, thermal structure, melting, and pathways of melt transport. The model is based on canonical statements of

conservation of mass, momentum, and energy for partially molten mantle (8, 9) and has previously been used to simulate mid-ocean ridge dynamics with homogeneous (10) and heterogeneous (11) mantle composition. It predicts time scales of melt transport that are consistent with those estimated from ²³⁰Th disequilibrium in young lavas (12). In the present work, the model is used to predict crustal thickness time-series arising from changes in sea level (Fig. 1) (13)

A suite of nine model runs for three permeability scales and three spreading rates was driven over a 5 My period using a Plio-Pleistocene sea-level reconstruction (14). Crustal curves from simulations with larger permeability and faster spreading rate contain relatively more high-frequency content than lower permeability and slower spreading rate runs (Fig. 1). Our model results contradict the previous scaling arguments (6, 7) in not showing a simple decrease in the sea level effect on ridge magmatism with increasing spreading rate.

To better understand these numerical results, we carried out an analysis of leading-order processes using a reduced complexity model. This model provides a solution for crustal thickness response to changes in sea level, approximating the results of the full numerical model, but with greater transparency. Assuming that all melt produced by sea level change is focused to the ridge axis, we obtain a magmatic flux in units of kg/year per meter along the ridge of

$$M_{\text{SL}}(t) = \int_{z_m}^0 x_i(z) \frac{\rho_w}{\rho_m} \Pi \dot{S}[t - \tau(z)] dz \quad (1)$$

where ρ_w/ρ_m is the density ratio of sea water to mantle rock, Π is the adiabatic productivity of upwelling mantle (in kg of melt per m^3 of mantle per meter of upwelling), $x_i(z)$ is the half-width of the partially molten region beneath the mid-ocean ridge at a depth z , and z_m is the maximum depth of silicate melting beneath the ridge. Most importantly, $\dot{S}[t - \tau(z)]$ is the rate of sea-level change τ years before time t (13).

This formulation reveals why our numerical model results (Fig. 1) contradict earlier work (6, 7). Whereas earlier work noted that variations in crustal thickness are inversely proportional to spreading rate, $C_{\text{SL}} = M_{\text{SL}}/(U_0\rho_c)$, our model shows that mass flux is proportional to the width of the partially molten region beneath the ridge. This width can be expressed as $x_i(z) = U_0R(z)/(4\kappa)$, where U_0 is the half-spreading rate, κ is the thermal diffusivity, and $R(z)$ accounts for depth dependent influences on melting that are independent of spreading rate (fig. S1). The competing influences associated with the volume of mantle from which melt is extracted and the rate at which new crust is formed means that sensitivity to sea level variation does not simply decrease with increasing spreading rate.

Instead, the magnitude of the crustal response depends upon the timescale of sea level forcing relative to the time required to deliver melt from depth to the surface. Melt delivery times τ are computed in the reduced model using a one-dimensional melt column formulation, and decrease with higher permeability and faster spreading rate (13, 15). The same response occurs in the numerical model; in both cases, τ decreases with increasing spreading rate because the background melting rate, dynamic melt fraction, and permeability of the melting region all increase.

To quantify crustal response as a function of timescale, we use the amplitude ratio of crustal to sea-level variation, called admittance, computed at discrete frequencies by applying sinusoidal forcing. Admittance curves for both the numerical (Fig. 2A) and reduced (Fig. 2B) models show a distinct maximum that shifts toward higher frequencies and larger magnitudes with shorter τ . When the period of sea-level forcing is short relative to the characteristic transport time $\tau_m = \tau(z_m)$, additional melt produced at depth (falling sea-level phase) does not have time to reach the surface before a negative perturbation to melt production occurs (rising sea-level phase); positive and negative perturbations cancel and crustal variation is small. When forcing periods are long relative to τ_m , melt perturbations reach the surface but are again small because melt production scales with the rate-of-change of sea level. Forcing periods near τ_m give maximum admittance because of a combination of large perturbation of melting rates and sufficient time to reach the surface (Fig. 2C). These results suggest that ridges are tuned according to melt-transport rates to respond most

strongly to certain frequencies of sea-level variability.

The correspondence of the results from the numerical and reduced models provides a sound basis for investigating the potential effects of sea level change on sea floor bathymetry. Variations in melt production lead to variations in crustal thickness and, through isostatic compensation, such thickness variations should produce changes in bathymetry identifiable in high-resolution surveys. The prominent spectral peaks of late Pleistocene sea level variation at the approximately $1/100 \text{ ky}^{-1}$ ice age, $1/41 \text{ ky}^{-1}$ obliquity, and $1/23 \text{ ky}^{-1}$ precession frequencies (16) therefore translate into a prediction for a bathymetric response that depends on permeability and spreading rate.

Our model results suggest that the best chance to detect a sea level response between $1/100 \text{ ky}^{-1}$ to $1/20 \text{ ky}^{-1}$ frequencies is at intermediate spreading ridges. Slow spreading ridges show little precession response, an obliquity response that is sensitive to uncertainties in permeability, and the effects of intense normal faulting. Such faulting causes rift valleys with larger relief than expected from sea-level induced melting variations. The sea-level signal should be less polluted by tectonic effects at fast-spreading ridges, but may have peak admittances at frequencies higher than $1/20 \text{ ky}^{-1}$ that would obscure the responses at predicted frequencies. For example, the numerical simulation with the fastest spreading and highest permeability has peak spectral energy at frequencies above precession (Fig. 1B).

At intermediate half-spreading rates of 3 cm/year , 40-ky periods lead to predicted bathymetric variations with a wavelength of 1200 m on each side of the ridge. Such fine-scale variations can be obscured in global topographic databases that grid data from multiple cruises and may have offsets in navigation or depth. To investigate the model predictions, a modern data set with uniform navigation and data reduction from a single survey is preferred. Such data are available for two areas of the Australian-Antarctica ridge that were surveyed by the icebreaker Araon of the Korean Polar Research Institute in 2011 and 2013 (Fig. 3).

Analysis is undertaken by identifying a region whose abyssal hill variability is relatively undisturbed by localized anomalies, averaging off-axis variability into a single bathymetric line, and converting off-axis distance into an estimate of elapsed time using a plate motion solution (17). Spectral analysis of the associated bathymetry time-series is performed using the multitaper procedure (18) and shows spectral peaks that are significant at an approximate 95% confidence level near the predicted ice age, obliquity, and precession frequencies (Fig. 3). Although absolute ages are uncertain because we lack seafloor magnetic reversal data, spectral analysis only requires constraining the relative passage of time. The two-sigma uncertainties associated with relative Australian-Antarctic plate motion are $\pm 4\%$ (17), implying, for example, that the $1/41 \text{ ky}^{-1}$ obliquity signal resides in a band from $1/39 \text{ ky}^{-1}$ to $1/43 \text{ ky}^{-1}$, a width that is smaller than our spectral resolution.

Another check on model–data consistency is to compare magnitudes of variability. Surface bathymetry will be roughly 6/23rds of the total variation in crustal thickness due to the relative density differences of crust–water and crust–mantle, assuming conditions of crustal isostasy. The closest match between simulation results and observations, in terms of the distribution of spectral energy, is achieved by specifying a permeability at 1% porosity of $K_0 = 10^{-13} \text{ m}^2$ (Fig. 3). The standard deviation of the simulated bathymetry is 36 m, after multiplying crustal thickness by 6/23 and filtering (13). To minimize the contribution from non-sea-level induced variations in the observed bathymetry, it is useful to filter frequencies outside of those between $1/150^{-1}$ and $1/10 \text{ ky}^{-1}$. The standard deviation of the filtered observations is 44 m, where the slightly larger value is consistent with changes in sea level being an important but not exclusive driver of changes in crustal thickness.

Analysis of bathymetry in another area of the Australian–Antarctic ridge 400 km to the southeast (fig. S2) shows a significant spectral peak at the obliquity frequency and indication of a peak near $1/100 \text{ ky}^{-1}$, but no peak near the precession frequencies. Predicted and observed bathymetry is also similar with standard deviations of 33 m and 34 m, respectively, after accounting for fractional surface expression and filtering. Absence of a precession peak may result from spectral estimates being more sensitive to elapsed time errors at higher frequencies (19), where such errors may be introduced through extensional faulting or asymmetric spreading. Detection could also be obscured by the previously noted influence of faulting (3, 20) as well as off-axis volcanism or sediment infilling of abyssal troughs. Detection of significant spectral peaks at predicted frequencies at two locations of the Australian–Antarctic ridge nonetheless constitutes strong evidence for modulation of crustal production by variations in sea level.

Our numerical and analytical results show a complex relationship between spreading rate and amplitudes of crustal thickness variations associated with changes in sea level. Perturbations to the background melt production and delivery depend on the frequency content of the sea-level signal, as a result of the dynamics of magma transport. Reference mantle permeability and ridge spreading rate are key controls on this frequency dependence. This result could be useful: the spreading rate can be accurately determined for a ridge, but parameters associated with magma dynamics are far less certain, such as the amplitude and scaling of permeability. Uncertainty associated with spectral estimates of bathymetry and sea level estimates need to be better characterized, but together these may provide a constraint on the admittance and, thereby, dynamical parameters of a ridge.

Although results from the high-resolution bathymetry are promising, much remains to be done to further test the hypothesis advanced here. Crustal thickness is not an instantaneous response to melt delivery from the mantle, but

also reflects crustal processes that may introduce temporal and spatial averaging. Where long-lived magma chambers are present, for example, there may also be a crustal time-averaging that depends on spreading rate. In addition, faulting at all spreading rates is an observed and important phenomenon and sea-floor bathymetry reflects the combined effects of magma output and crustal faulting (3, 20). Deconvolving the relative roles of such processes will be important. High-resolution surveys in targeted regions will provide the opportunity for a more complete and rigorous analysis than is presently possible.

REFERENCES AND NOTES

1. H. Menard, J. Mammerrickz, Abyssal hills, magnetic anomalies and the east pacific rise. *Earth Planet. Sci. Lett.* **2**, 465–472 (1967). doi:10.1016/0012-821X(67)90191-4
2. D. Scheirer, K. C. Macdonald, D. W. Forsyth, S. P. Miller, D. J. Wright, M.-H. Cormier, C. M. Weiland, A map series of the Southern East Pacific Rise and its flanks, 15° S to 19° S. *Mar. Geophys. Res.* **18**, 1–12 (1996). doi:10.1007/BF00286201
3. K. Macdonald, P. Fox, R. Alexander, R. Pockalny, P. Gente, Volcanic growth faults and the origin of Pacific abyssal hills. *Nature* **380**, 125–129 (1996). doi:10.1038/380125a0
4. J. Goff, Y. Ma, A. Shah, J. Cochran, J. Sempere, Stochastic analysis of seafloor morphology on the flank of the Southeast Indian Ridge: The influence of ridge morphology on the formation of abyssal hills. *J. Geophys. Res.* **102** (B7), 15521 (1997). doi:10.1029/97JB00781
5. E. Kappel, W. Ryan, Volcanic Episodicity and a Non-Steady State Rift Valley Along Northeast Pacific Spreading Centers: Evidence From Sea MARC I. *J. Geophys. Res.* **91** (B14), 13925 (1986). doi:10.1029/JB091iB14p13925
6. P. Huybers, C. Langmuir, Feedback between deglaciation, volcanism, and atmospheric CO₂. *Earth Planet. Sci. Lett.* **286**, 479–491 (2009). doi:10.1016/j.epsl.2009.07.014
7. D. C. Lund, P. D. Asimow, Does sea level influence mid-ocean ridge magmatism on Milankovitch timescales? *Geochem. Geophys. Geosyst.* **12**, 12009 (2011). doi:10.1029/2011GC003693
8. D. McKenzie, The Generation and Compaction of Partially Molten Rock. *J. Petrol.* **25**, 713–765 (1984). doi:10.1093/petrology/25.3.713
9. R. Katz, *J. Petrol.* **49**, 2099 (2008).
10. R. Katz, *Geochem. Geophys. Geosys.* **10**, Q0AC07 (2010).
11. R. Katz, S. Weatherley, Consequences of mantle heterogeneity for melt extraction at mid-ocean ridges. *Earth Planet. Sci. Lett.* **335–336**, 226–237 (2012). doi:10.1016/j.epsl.2012.04.042
12. A. Stracke, B. Bourdon, D. McKenzie, Melt extraction in the Earth's mantle: Constraints from U–Th–Pa–Ra studies in oceanic basalts. *Earth Planet. Sci. Lett.* **244**, 97–112 (2006). doi:10.1016/j.epsl.2006.01.057
13. Materials and methods are available as supplementary materials on Science Online.
14. M. Siddall, B. Hönisch, C. Waelbroeck, P. Huybers, Changes in deep Pacific temperature during the mid-Pleistocene transition and Quaternary. *Quat. Sci. Rev.* **29**, 170–181 (2010). doi:10.1016/j.quascirev.2009.05.011
15. I. Hewitt, Modelling melting rates in upwelling mantle. *Earth Planet. Sci. Lett.* **300**, 264–274 (2010). doi:10.1016/j.epsl.2010.10.010
16. J. D. Hays, J. Imbrie, N. J. Shackleton, Variations in the Earth's Orbit: Pacemaker of the Ice Ages. *Science* **194**, 1121–1132 (1976). Medline doi:10.1126/science.194.4270.1121
17. C. DeMets, R. G. Gordon, D. F. Argus, Geologically current plate motions. *Geophys. J. Int.* **181**, 1–80 (2010). doi:10.1111/j.1365-246X.2009.04491.x
18. D. Percival, A. Walden, *Spectral Analysis for Physical Applications: Multitaper and Conventional Univariate Techniques* (Cambridge University Press, 1993).
19. P. Huybers, C. Wunsch, A depth-derived Pleistocene age model: Uncertainty estimates, sedimentation variability, and nonlinear climate change. *Paleoceanography* **19**, PA1028 (2004). doi:10.1029/2002PA000857
20. W. R. Buck, L. L. Lavier, A. N. Poliakov, Modes of faulting at mid-ocean ridges. *Nature* **434**, 719–723 (2005). Medline doi:10.1038/nature03358
21. J. F. Rudge, D. Bercovici, M. Spiegelman, Disequilibrium melting of a two phase

- multicomponent mantle. *Geophys. J. Int.* **184**, 699–718 (2011). [doi:10.1111/j.1365-246X.2010.04870.x](https://doi.org/10.1111/j.1365-246X.2010.04870.x)
22. S. Balay et al., <http://www.mcs.anl.gov/petsc> (2001).
23. R. Katz, M. Knepley, B. Smith, M. Spiegelman, E. Coon, Numerical simulation of geodynamic processes with the Portable Extensible Toolkit for Scientific Computation. *Phys. Earth Planet. Inter.* **163**, 52–68 (2007). [doi:10.1016/j.pepi.2007.04.016](https://doi.org/10.1016/j.pepi.2007.04.016)
24. M. Tabor, *Chaos and Integrability in Nonlinear Dynamics: An Introduction* (Wiley, 1989).
25. G. Batchelor, *An Introduction to Fluid Mechanics* (Cambridge University Press, 1967).
26. D. Turcotte, G. Schubert, *Geodynamics* (Cambridge University Press, 2002).
27. N. Ribe, The deformation and compaction of partial molten zones. *Geophys. J. R. Astron. Soc.* **83**, 487–501 (1985). [doi:10.1111/j.1365-246X.1985.tb06499.x](https://doi.org/10.1111/j.1365-246X.1985.tb06499.x)
28. I. Hewitt, A. Fowler, Melt channelization in ascending mantle. *J. Geophys. Res.* **114** (B6), B06210 (2009). [doi:10.1029/2008JB006185](https://doi.org/10.1029/2008JB006185)
29. D. Sparks, E. Parmentier, Melt extraction from the mantle beneath spreading centers. *Earth Planet. Sci. Lett.* **105**, 368–377 (1991). [doi:10.1016/0012-821X\(91\)90178-K](https://doi.org/10.1016/0012-821X(91)90178-K)

ACKNOWLEDGMENTS

The research leading to these results has received funding from the European Research Council under the European Union's Seventh Framework Programme (FP7/2007–2013) / ERC grant agreement number 279925 and from the U.S. National Science Foundation under grant 1338832. It is a part of project PP13040 and PE14050 funded by the Korea Polar Research Institute. Crowley thanks J. Mitrovica and Katz thanks the Leverhulme Trust for additional support. Numerical models were run at Oxford's Advanced Research Computing facility. Bathymetry data are included in the Supplementary Materials.

SUPPLEMENTARY MATERIALS

www.sciencemag.org/content/science.1261508/DC1

Figs. S1 to S3

Table S1

References (21–29)

Data Files KR1 and KR2

22 September 2014; accepted 28 January 2015

Published online 5 February 2015

10.1126/science.1261508

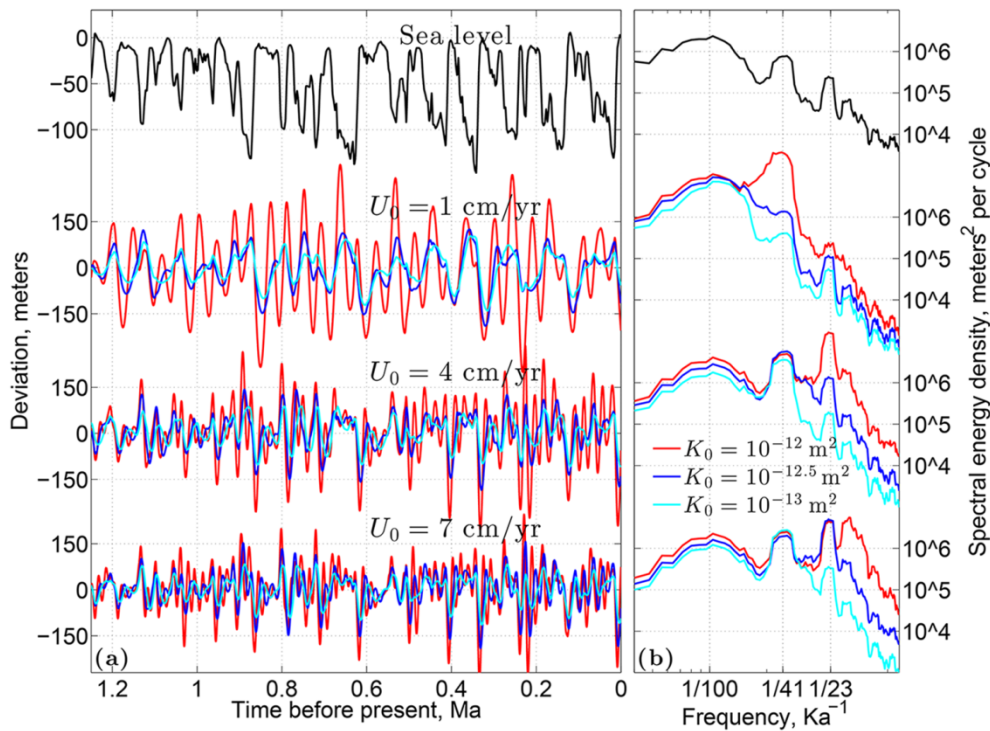


Fig. 1. Simulated bathymetric relief driven by Plio-Pleistocene sea-level variation. (A) Imposed sea-level variation (black) and predicted bathymetric relief (color) for the past 1.25 Ma from simulations at three half-spreading rates U_0 and three permeability levels K_0 . Isostatic compensation is assumed to scale the amplitude of crustal thickness variation by $6/23$ to give bathymetric relief. Permeability in the simulations is computed by applying $K(x,z) = K_0(\varphi/\varphi_0)^3 \text{ m}^2$ to the porosity field $\varphi(x,z)$, where $\varphi_0 = 0.01$ is a reference porosity. Cyan, blue, and red lines correspond to $\log_{10}K_0 = -(13, 12.5, 12)$, respectively. (B) Power spectral density estimates for each time-series, made using the multitaper method with seven tapers. Axes are logarithmic.

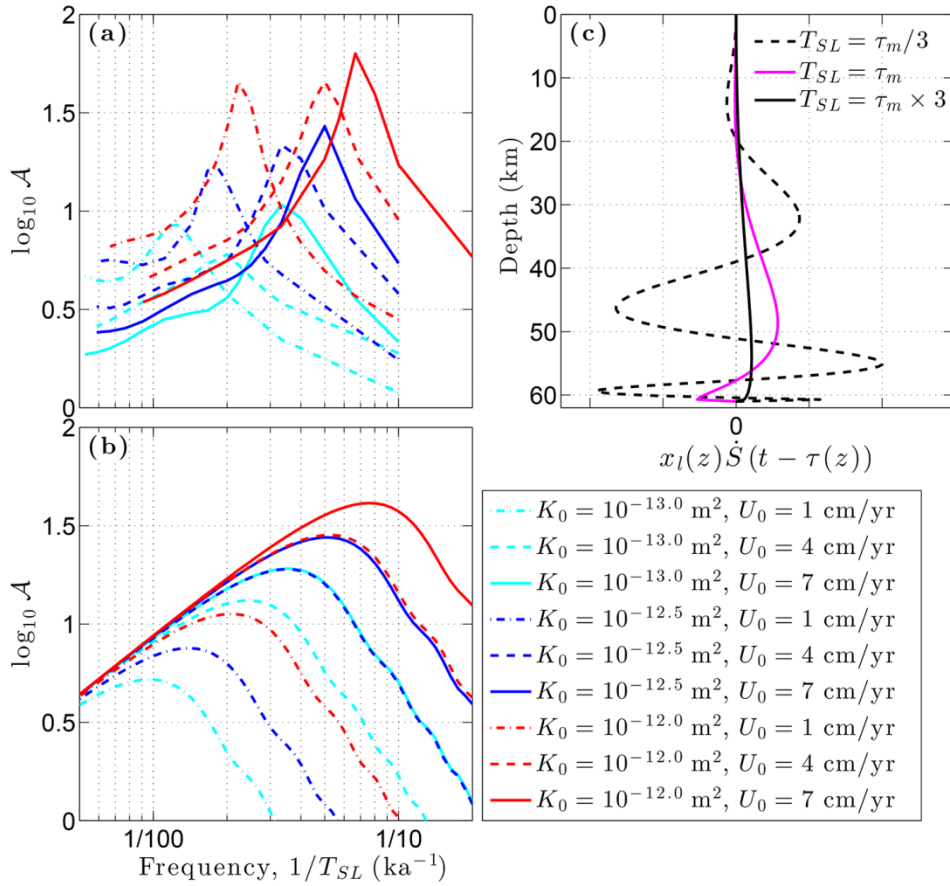


Fig. 2. Crustal thickness admittance, computed for a sinusoidal variation in sea level with period T_{SL} . Admittance curves derived from (A) numerical simulations and (B) the reduced model (13). (C) A plot of depth z versus the integrand from the reduced model of magma production due to sea-level variation, $M_{SL}(t) \propto \int_{-z_m}^0 x_l(z) \dot{S}[t - \tau(z)] dz$ (see also Eq. 1 and text following). The model is evaluated for for $U_0 = 4 \text{ cm/year}$, $K_0 = 10^{-13} \text{ m}^2$, and three values of sea-level oscillation period T_{SL} .

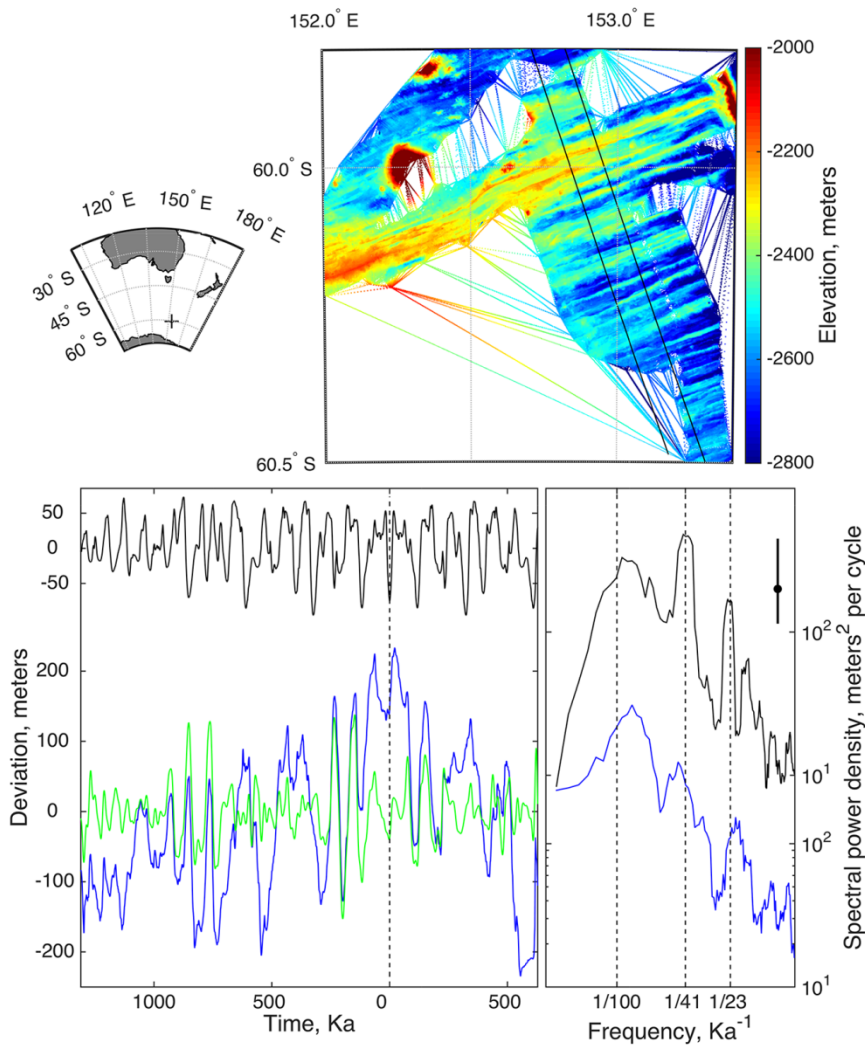


Fig. 3. Bathymetry at a section of the Australian-Antarctic Ridge. A region of consistent bathymetry is indicated between the black lines (top right) and is shown in profile (bottom left, blue) after converting off-axis distance to an estimate of time. Time is zero at the approximate ridge center. Also shown is bathymetry after filtering frequencies outside of $1/150 \text{ ky}^{-1}$ and $1/10 \text{ ky}^{-1}$ (green), and simulated bathymetry (black, for $U_0 = 3.3 \text{ cm/year}$ and $K_0 = 10^{-13} \text{ m}^2$). Spectral estimates (bottom right) are shown for the unfiltered bathymetry (blue) and model results (black), where the latter are offset upward by an order of magnitude for visual clarity. Data availability is uneven across the ridge, and spectral estimates are for the longer, southern flank. Note that unlike in Fig. 1B, spectral estimates are prewhitened in order to improve the detectability of spectral peaks (see supplementary material). Vertical dashed lines indicate frequencies associated with 100ky late-Pleistocene ice ages, obliquity, and precession. Axes are logarithmic. Statistical significance is indicated by the black bar at the top right of the panel: spectral peaks rising further than the distance between the mean background continuum (corresponding to the black dot) and 95th percentile (top of black bar) are significant.